Room-Temperature Processable TiO$_2$ Solar Paint for Dye-Sensitized Solar Cells

Anurag Roy [1,*] , **Shubhranshu Bhandari** [1,*] **and Tithi Sen** [2]

1   Solar Energy Research Group, Environment and Sustainability Institute, Penryn Campus, University of Exeter, Cornwall TR10 9FE, UK
2   Department of Chemistry and Chemical Biology, Indian Institute of Technology (Indian School of Mines), Dhanbad 826004, India; 19tsen@gmail.com
*   Correspondence: a.roy30@exeter.ac.uk (A.R.); s.bhandari@exeter.ac.uk (S.B.)

Abstract: Dye-sensitized solar cells (DSSCs) have emerged as promising alternatives to traditional silicon photovoltaics owing to their environmentally friendly nature, easy preparation, and low cost. However, a critical bottleneck in DSSC fabrication lies in the high-temperature treatment required for the metal-oxide, primarily titanium dioxide (TiO$_2$), photoanode. This study presents an advanced approach aimed at overcoming this challenge by developing a facile and cost-effective room temperature processable TiO$_2$ paste for large-scale device production and commercialization. In our investigation, TiO$_2$ nanoparticles were synthesized using the sol-gel hydrothermal method. The resulting material served as the basis for a solar paint formulation, utilized as a precursor for the photoanode in tertiary butyl alcohol. Applying this paint, achieved with a simple paintbrush, eliminated the need for high-temperature curing, binders, and reduced chemical additives. This minimizes energy consumption during fabrication and enhances the interface quality and charge transport properties of the photoanode, as evidenced by photovoltaic impedance spectroscopy measurements.

Keywords: DSSC; photoanode; photovoltaic; solar paint; TiO$_2$

1. Introduction

The growing energy demand, efforts to limit climate change, and steps toward carbon neutrality have greatly influenced the research community on power generation via sustainable energy technologies. Counting on the current global power demand, finding efficient and cost-effective solar power generation systems to replace traditional fossil fuels is essential for a sustainable society. Propitious advances have been noticed over the years, with the progression of first generation (silicon photovoltaics), second generation (CdTe, CIGS, etc.), and emerging photovoltaic (PV) systems (dye-sensitized, perovskite, quantum dot, solar cells, etc.) [1–7].

Only a minuscule fraction of global energy consumption, accounting for less than 0.05% in 2004, is derived from solar cells due to the exorbitant costs associated with the prevailing technology based on crystalline silicon. Dye-Sensitized Solar Cells (DSSC) emerge as a prominent alternative to silicon PVs, constituting the focal point of the proposed investigation. DSSCs are intricate systems comprising a nanocrystalline titanium dioxide (TiO$_2$) semiconductor with a dye adsorbed on it, an electrolyte solution capable of reduction and oxidation, and a transparent electrode.

Mass-produced DSSCs currently achieve an efficiency of approximately 7%, with the aspiration to attain a target efficiency of 15% or higher, rendering this technology viable for large-scale electricity generation. Ongoing enhancements in DSSC performance hinge on developing novel dyes and electrolytes. Presently, no predictive theories facilitate the systematic enhancement of DSSCs, with efficiency improvements largely reliant on chemical intuition and systematic exploration.

The emerging PVs, due to their ease of fabrication, are the most experimented devices these days, and DSSC is one of the leaders in overcoming 13% power conversion efficiency (PCE) [8–12]. Besides, DSSCs are environmentally benign compared to traditional PVs, and produce excellent performance under diffused light [13,14]. The development of novel synthesis technologies, nanostructured materials, and refinement processes brings new insight into the field of DSSCs [15,16]. The soul of DSSC comprises a photoelectrochemical cell sandwiching two electrodes and an electrolyte under light-induced redox reactions [17]. Numerous efforts have been attempted to assist the DSSC to the next level, such as the decoration of noble metals, ion doping, refinement with metal oxides, development of different dyes, modifications with up/down conversion materials, investigation of various counter electrodes, using different electrolytes, developing perovskite oxide photoanodes, and utilization of composites and polymers [18,19]. TiO_2 has been most widely used as a photoanode, alongside various scattering layers. Passive electron mobility, charging carrier recombination at the interfaces between the electrolyte and metal oxide, possible complex formation by metal ion-dye interaction, high absorption time of dyes, and counter electrode degradation are genuine obstructions that limit DSSC performance [20–23]. Diverse perovskite oxides (POs) have emerged as feasible options for DSSC photoanodes, since they have intriguing photophysical characteristics and can be synthesized via simple and low-cost methods in a conventional laboratory [24]. Among the alternative photoanode materials, different Ba- and Sr-based ternary POs, such as $BaSnO_3$, $SrSnO_3$, $BaTiO_3$, and $SrTiO_3$, have demonstrated their potential in the DSSC field [25–27].

The pursuit of material scientists has long been centered on the coveted objective of devising PV technologies that are both cost-effective and reasonably efficient. Despite being the most vital component of DSSC from a PCE and stability perspective, TiO_2 has the challenge of improving further [28,29]. One of the most popular precursors of producing TiO_2 paste is based on a sol-gel Pechini method [23].

In this regard, strategies that can enrich the interface quality and electron transport properties are a matter of concern, which brings about new ideas to develop the paste and deposition of the films [30]. The deposition techniques are mainly divided into two categories, namely, physical and chemical approaches. Atomic layer deposition (ALD), spray pyrolysis, chemical vapor deposition (CVD), electrochemical deposition (ECD), and all their variants are the most famous chemical deposition methods [31]. On the other hand, casting, spin coating, dip coating, electrospray deposition (ESD), and physical vapor deposition (PVD) are among the most considered physical deposition pathways [32]. However, other than physical and chemical deposition methods, a large section of distinguished approaches are known as printing and coating techniques, such as screen-printing, pad printing, doctor blading, slot die, roll-to-roll method, inkjet printing, gravure printing, flexographic printing, and rotary screen-printing [33]. Screen-printed DSSC has achieved an efficiency of >8% for a 100 cm^2 device area [34,35]. The doctor blading method recorded an efficiency of >8% for mini modules [36]. Reports indicate inkjet-printed devices have produced an efficiency of >6% to date with printed electrolytes and photoanodes [37,38]. Several researchers worldwide have utilized roll-to-roll, gravure printing, and flexographic printing methods in recent years. Alongside the printing and coating techniques, the nature of the precursors of the electrode materials is quite important to determine the quality of the device as it controls the charge transport property at the interfacial contacts [39]. Scientists utilize different pastes with various binders to improve the film quality. Also, the annealing temperature, in this respect, influences the device's performance [40]. In the year 2007, Arakawa et al. reported a noteworthy achievement with an efficiency of 7.4% under room-temperature processing, albeit under high-pressure conditions (100 MPa) [41]. More recently, Liu et al. demonstrated an efficiency of 2.05% for a TiO_2 film prepared at 85 °C, while compression at 1 ton elevated the efficiency to 5.86%, employing an organic dye on plastic substrates [42]. Agarkar et al. successfully engineered a TiO_2 solar paint with a conversion efficiency of 3.6% on FTO/glass substrates. Notably, this achievement was

realized through fully room-temperature processing, including the utilization of a flexible substrate [43].

Despite these significant achievements, subsequent research endeavors in the realm of room-temperature solar paint incorporating TiO_2 have been notably scarce. This underscores the importance of further research analysis, as the present work represents a pioneering approach, potentially offering insights for future developments in this domain. In fabricating photoanodes for DSSC, TiO_2 is commonly employed, typically in conjunction with binders such as ethyl cellulose and alpha terpinol. These binders serve to form a paste from the synthesized TiO_2 powder. Subsequent to this application, the photoanode necessitates a calcination process at >400 °C to ensure the complete removal of these binders. However, this additional heating step consumes energy and poses a risk of cracking or delamination of the TiO_2 from the glass substrate at elevated temperatures. Conventional methods involve screen-printing or doctor blading to fabricate the photoanode, which are time-consuming and labor-intensive processes. To streamline the production of DSSC devices and facilitate ease of analysis, we have developed a room-temperature TiO_2 paste. This paste can be directly applied to a FTO glass substrate using screen-printing, akin to a painting application, eliminating the need for additional high-temperature processing. The resultant TiO_2 paste is deemed "room temperature processable," allowing for direct utilization without requiring additional heating at elevated temperatures. The observation indicates a significant increase of ~11% in the current density for the DSSCs with solar paint compared to devices based on commercial TiO_2 paste.

This innovation saves time and addresses the environmental impact associated with energy-intensive fabrication processes. This simplified and accessible approach to DSSC photoanode fabrication contributes to energy conservation and environmental sustainability.

2. Experimental Section

2.1. Materials

Titanium isopropoxide (TTIP, 97%), Oleic acid, triethanolamine (TEOA), sodium hydroxide (NaOH), tertiary butyl alcohol (tBA), and ethanol was obtained from Merck Life Science UK Limited, Gillingham, UK and used as received.

2.2. Preparation of Sodium Oleate

Sodium oleate was prepared using the same method reported in the earlier work [44]. Briefly, 16 g of NaOH was added to ethanol (200 mL) and stirred at ~60 °C to dissolve it completely. Then, 20 mL of oleic acid was added to the solution, and stirring was continued for 2 h. The as-obtained yellowish-white precipitate was centrifuged (5000 rpm), followed by washing with hexane, which removed excess oleic acid from the precipitate. After that, the yellowish-white product was dried at 70 °C for 12 h.

2.3. Synthesis of TiO_2 Nanoparticles

The synthesis was adopted from the previous report with suitable modification [45]. In a controlled environment, a primary stock solution of Ti^{4+} was synthesized by amalgamating TTIP with TEOA, adhering to a molar ratio of TTIP:TEOA = 1:2. This proportion was chosen to circumvent the rapid hydrolysis of Ti^{4+}. Subsequent to this process, deionized water (DI) was integrated to achieve a concentration of 0.5 mol dm^{-3} in Ti^{4+}. In the ensuing step, 0.02 mol/dm^3 of sodium oleate was amalgamated with the aforementioned stock solution, ensuring consistent stirring throughout. To achieve optimal conditions, the pH of this composite was fine-tuned to 10 ± 0.5, and the cumulative volume of the stock solution was adjusted to reach 30 mL. This resultant blend was then relocated to a sealed flask, undergoing an aging process for 24 h at a temperature of 100 °C, facilitating gelation. In the terminal phase, the dense gel was transferred to a Teflon-coated autoclave and underwent an aging process at 140 °C for 72 h. This meticulous procedure culminated in the nucleation and growth of the desired titania nanoparticles (TNPs). After introducing the specified quantity of TNPs into tBA at a 4:1 ratio, the mixture was consistently agitated for an ex-

tended period. This process yielded a thick paste that exhibited characteristics akin to paint. Previous investigations have highlighted the use of tBA and water as solvents for synthesizing binder-free TiO_2 pastes, resulting in a well-connected TiO_2 matrix [43]. The water generated incidentally during this synthesis is typically removed through annealing at temperatures above 120 °C. By introducing H^+ ions via acid addition, maintaining a pH of ~2, the formation of the TiO_2 matrix is catalyzed, with water produced as a byproduct. This approach expedites the paste's viscosity development, achieving it within hours, whereas conventional techniques often take 4–5 days. Following this, a complex between tBA and water forms, where the water molecules envelop the excess tBA molecules. Remarkably, the water's volume is consistently half that of tBA. Under these conditions, the complex can be efficiently removed at ambient temperatures.

2.4. Fabrication of Device Using Room-Temperature TiO_2 Solar Paint

First, the standard etching and cleaning process of fluorine-doped tin oxide (FTO)/glasses were carried out. The synthesized TNP paint was uniformly coated onto FTO with a sheet resistance of 12 Ω/cm^2 by simply applying the solar paint using the screen-printing technique. The printing method was utilized to deposit the layers multiple times, depending on the device type. TiO_2 films of varying thicknesses were achieved by implementing multiple layers of the paint. Following the deposition, the films were dried at ambient conditions and subsequently immersed in a 0.5 mM N719 dye [Di-tetrabutylammonium cis-bis(isothiocyanato)bis(2,2′-bipyridyl-4,4′-dicarboxylato) ruthenium(II)] solution. The DSSCs' counter electrode system was fabricated using a platinum (Pt) catalyst-coated top electrode on FTO and an iodide-tri-iodide electrolyte. In detail, N719 dye solution was prepared in ethanol with a concentration of 0.5 Mm, which was stored in a sealed container away from sunlight for 24 h before use. The TiO_2-coated FTO slides were immersed in the dye solutions for selective times for dye adsorption onto the metal oxide surface. After removing, the FTO slides were immediately rinsed with ethanol, to wash out the excess dye that had adhered to the surface and dried with nitrogen flow. A small hole with a diameter of 0.5 mm was made on the FTO/commercial TiO_2 glass slide. The cleaned substrate was heated at 450 °C for 15 min to remove any residual organic contaminants. Pt was deposited on the FTO glass by brush-painting a thin layer or by drop-casting 1–2 drops of the light-sensitive Platisol T solution. The deposited layer was gradually air dried followed by heating at 450 °C for 15 min to activate the platinum layer for working. Sandwich-type DSSCs were assembled by utilizing a platinized Fluorine-doped Tin Oxide (FTO) substrate, deposited with a hot-melt film (~25 μm, Surlyn, Dyesol) and the dye-adsorbed titania film. The assembly involved drop-casting the components. For the electrolyte preparation, a solution of 0.3 M 1-methylbenzimidazole (NMB) was thoroughly mixed with an equal volume ratio of acetonitrile and 3-methoxypropionitrile (MPN). This mixture was supplemented with 0.4 M LiI, 0.4 M tetrabutylammonium iodide (TBAI), and 0.04 M I_2, and the entire blend was stirred overnight. All chemicals used were sourced from Sigma-Aldrich and employed without further purification. Subsequently, the prepared I_3^-/I^- liquid electrolyte infiltrated the cell, constituting a sandwiched DSSC device. Six photoanodes' PV performances were evaluated, and the average values for their PV performances were determined. Each photoanode had an active area of 2.5 cm × 1.6 cm. Typically, in the conventional fabrication process of photoanodes for DSSCs, the mitigation of metal oxide agglomeration and grain growth, as well as the prevention of surface coating cracks, is achieved through slow heating and cooling cycles. Consequently, utilizing our developed solar paint eliminates the necessity for these prolonged processes, leading to considerable time and energy savings.

2.5. Materials and Device Characterization

X-ray diffraction (XRD) measurements were performed by X'pert pro MPD of PANalytical system (Malvern, UK) with CuK_α radiation (λ = 1.5406 Å). Tecnai G2 30ST (FEI, Hillsboro, OR, USA), 300 kV, was used for the bright-field image and high-resolution trans-

mission electron microscopy image (HRTEM). A Raman spectrophotometer STR500 (Cornes Technologies system using 514.5 nm Ar+ green laser with 50 mW power) was utilized for Raman mapping. TESCAN VEGA3 SEM was used for the FESEM (field emission scanning electron microscope) and EDX (energy-dispersive X-ray) characterization. The SEM images were further processed through MIPAR Image analyzer. The Quantachrome (iQ3) instrument determined the surface area of nanomaterials, and the Brunauer-Emmett-Teller (BET) theory was applied. Barrett-Joyner-Halenda (BJH) analysis can also be employed to determine pore size distribution nitrogen using adsorption and desorption techniques. SHIMADZU UV-3600 (Tokyo, Japan) was used for the absorbance spectra. X-ray photoemission spectroscopy (XPS) measurement was carried out by PHI 5000 Versa probe II scanning XPS microprobe (ULVAC-PHI, Chigasaki, Japan). EIS measurements were executed with an Metrohm AUTOLAB frequency analyzer equipped with a Frequency Response Analyzer (FRA) Module and AUTOLAB PGSTAT 101. The measurements were executed under the same solar simulator condition for all devices in the frequency range of 0.1 Hz to 100 kHz. All of the DSSCs were characterized at 0.70 V, which closely resembles the open-circuit voltage of the devices using NOVA 2.1 software. The experimental data were fitted using Z-view software (version 3.4d, Scribner Associates, Inc., Southern Pines, NC, USA) and a suitable equivalent circuit. Incident photon-to-electron conversion efficiency (IPCE) was conducted on a BENTHAM PVE300 Photovoltaic EQE (external quantum efficiency) and IQE (internal quantum efficiency) solution under 400–800 nm wavelength utilizing a tungsten halogen lamp source. Majority of these instruments belong to the University of Exeter's Central Characterization Facility, and we have utilized them for our work.

2.6. DSSC Testing

The PV performance of the assembled devices was assessed under an irradiance of 1000 W/m^2 using a Wacom AAA continuous solar simulator (model WXS-210S-20, AM 1.5 G). The I-V characteristics were recorded employing an EKO MP-160i I-V Tracer. Electrochemical Impedance Spectroscopy (EIS) measurements were conducted using an Autolab frequency analyzer setup, equipped with an Autolab PGSTAT 10 and a Frequency Response Analyzer (FRA) module. These measurements were performed under identical solar simulator conditions, ranging from 0.1 Hz to 100 kHz. All devices were measured at their open-circuit voltage (0.70 V). The experimental data were fitted using Z-view software (version 3.4d, Scribner Associates, Inc.), employing appropriate equivalent circuits. All presented data represent the average of measurements obtained from three different devices for each sample.

3. Results and Discussion

During the synthesis of TNPs, the transformation of the sol-gel method to produce the final product was observed by Raman mapping, as shown in Figure 1. The Raman mapping in Figure 1a demonstrates the as-prepared stock sample before the gelation process, where black spots imply the solvent in the sample. During the aging process of the sample transformation, the nature of the sample goes through Figure 1b,c, where the reduction of solvent and binders were observed. Figure 1d shows the solvent-free NPs after the terminal phase of autoclave heating. After the synthesis, chemical identification of the synthesized TiO$_2$ was carried out by XRD and XPS analysis. The XRD pattern of the synthesized TiO$_2$ displays the presence of broad peaks, as shown in Figure 2a. The reason behind broad peaks can be attributed to either the small crystallite size of the NPs or the semicrystalline nature of the TiO$_2$ [46]. The peaks at ~25°, 38°, 47°, 54°, 56°, 63°, 69°, and 75° resemble the anatase crystalline phase having (101), (004), (200), (105), (211), (204), (116), and (215) planes, respectively, (JCPDS 21-1272) of TiO$_2$ [36].
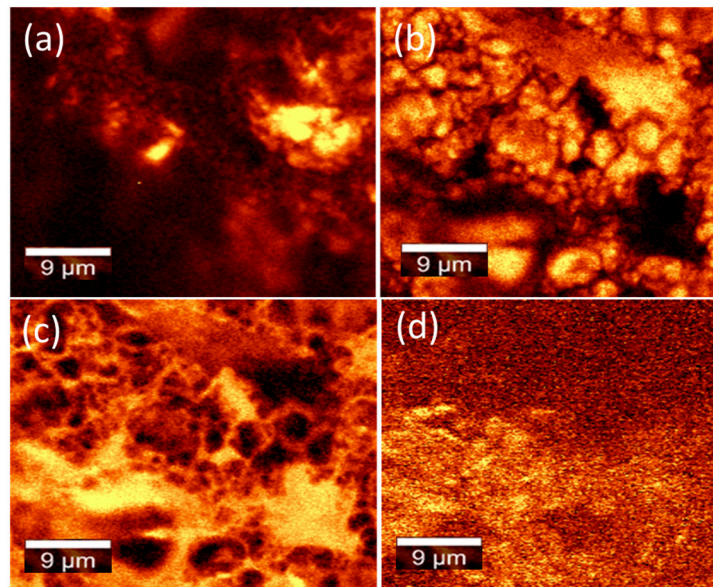
Figure 1. Raman mapping of samples during nanoparticle synthesis: (**a**) the stock solution, (**b**) the aging process, (**c**) gelation, and (**d**) final TiO$_2$ nanoparticles after autoclave, respectively.
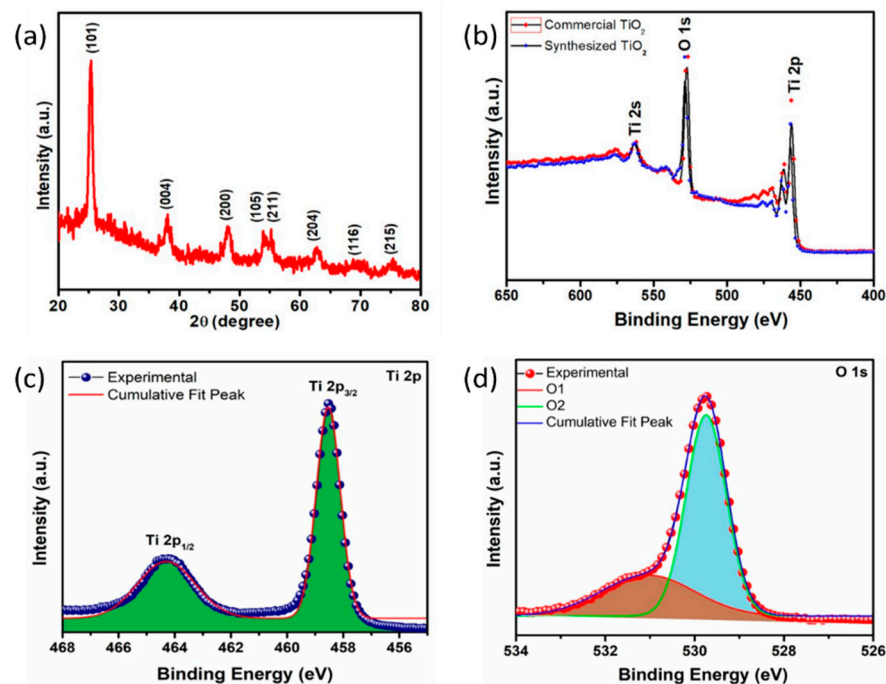
Figure 2. (**a**) X-ray diffraction pattern of TiO$_2$, (**b**) XPS survey spectrum of TiO$_2$, and (**c**,**d**) core level spectrum of Ti 2p and O1s for TiO$_2$ nanoparticles, respectively.

Noticeably, only the anatase phase was detected from the sample without any trace of the rutile phase, which indicates the presence of a low concentration of oxygen vacancies as the particle growth mechanism involved a high concentration of gaseous oxygen, which hinders the anatase to rutile transformation [47]. The XPS confirms the synthesized sample's oxidation state and elemental composition, as shown in Figure 2b–d. The peak positions of synthesized TiO$_2$ match well with the commercial product, as displayed in Figure 2b of the XPS survey spectrum. The characteristic double peaks were observed with binding energies of ~458.8 eV and 464.5 eV for the Titanium 2p$_{3/2}$ and 2p$_{1/2}$, respectively, as shown in Figure 2c. Conversely, Figure 2d shows the corresponding Oxygen 1s peak ~530 eV

due to the O^{2-} ion (O1 component). In contrast, the higher binding side O2 component indicates the chemisorbed oxygen in the grain boundaries [48].

After confirming the chemical identity and elemental states, the structural property of the TNPs was characterized by SEM-EDX. Figure 3a–d elucidates the SEM cross-sectional thickness measurements of a uniform photoanode. The increment in the number of layers correlates with an augmentation in photoanode thickness, ranging from ~3 μm to ~15 μm. Notably, the thickness results underscore the NPS' fine and homogeneous distribution across the surfaces.
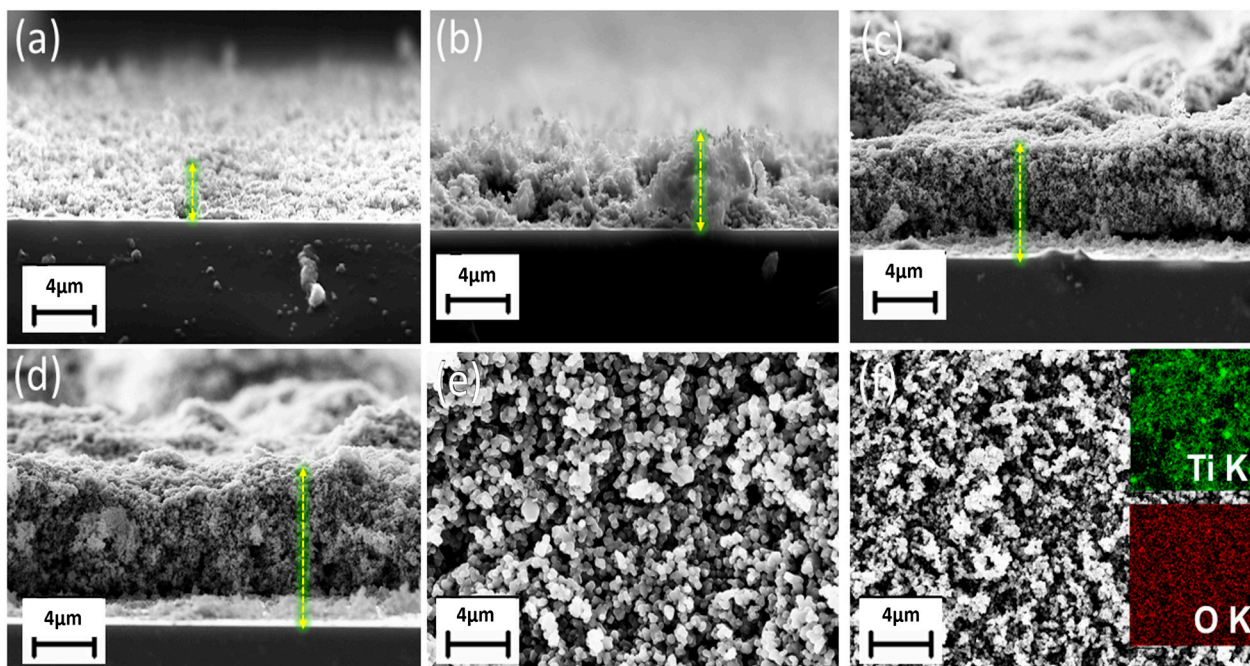
Figure 3. Scanning Electron Microscope (SEM) cross-sectional microstructure images depicting layer-dependent synthesized TNP solar paint photoanodes: (**a**) for 1 layer, (**b**) 2 layers, (**c**) 3 layers, and (**d**) 4 layers (highlighted by arrow). (**e**,**f**) SEM surface microstructural images of commercial TiO_2 and synthesized TNP, respectively (inset: corresponding EDX mapping analysis images).

Figure 3e presents the SEM microstructural surface image of the commercially available TNP paste photoanode, while Figure 3f depicts the corresponding surface SEM microstructure of our synthesized TiO_2 photoanode. It is evident from the images that our synthesized TNP exhibits finer particle size in comparison to its commercial counterpart, showcasing a homogeneous distribution across the surfaces. The synthesized TNPs revealed a highly favorable particle size for the room-temperature solar paint. The SEM image indicates ultrafine particles with an average grain size of ~20 nm, which clarifies the reason behind the broad peaks of XRD analysis [49]. The EDX mapping (inset of Figure 3f) also confirms the elements of the TiO_2 sample present as Ti and O, only. Notably, the impact of particle size distribution on the performance of DSSC is a matter of considerable significance. Specifically, the particle size of TiO_2 plays a pivotal role in determining both the surface area and pore size of NPs, thereby exerting direct influence over dye-loading [50]. In the context of wet chemical reactions, the formation of NPs facilitates the development of desired morphologies. Nevertheless, one-dimensional nanostructures exhibit superior improvements in DSSC efficiency due to the establishment of a direct conduction path for electron flow; however, they are not a straightforward synthesis specifically for large-scale consideration. It is imperative to note that three-dimensional structures in DSSCs, despite possessing a higher surface area compared to particles and rods, tend to be less efficient. This inefficiency can be attributed to the multiple trapping and de-trapping events of electrons occurring in the presence of inhomogeneous grain size boundaries. Consequently,

a nuanced interplay of particle size, morphology, and homogeneous distribution emerges as a critical determinant governing electron diffusion rate. When optimized, this intricate interdependence contributes significantly to enhancing DSSC efficiency [51].

For further structural characterization, TEM-SAED analysis was performed. The bright-field TEM images of the commercial TiO_2 paste are presented in Figure 4a, revealing particle sizes ranging from 20 to 50 nm. Moreover, these images exhibit a high level of crystallinity, as evidenced by the distinct lattice fringes of the (101) crystalline planes observed in the corresponding high-resolution TEM image (Figure 4b). The SAED pattern of the sample, depicted in Figure 4c, further underscores the pronounced crystallinity, elucidating the analytical phase of the specimen. The particle size of the synthesized TNP measured from the TEM (Figure 4d) was in the range of 15–30 nm, which is smaller and finer than commercial TiO_2 and is consistent with the SEM analysis. The high-resolution TEM image (Figure 4e) showcases the distinct lattice fringes corresponding to the (101) reflection, having a lattice spacing of 3.51 Å. The SAED pattern demonstrates the crystalline nature of the anatase TiO_2, implying different planes witnessed from the XRD, as displayed in Figure 4f.
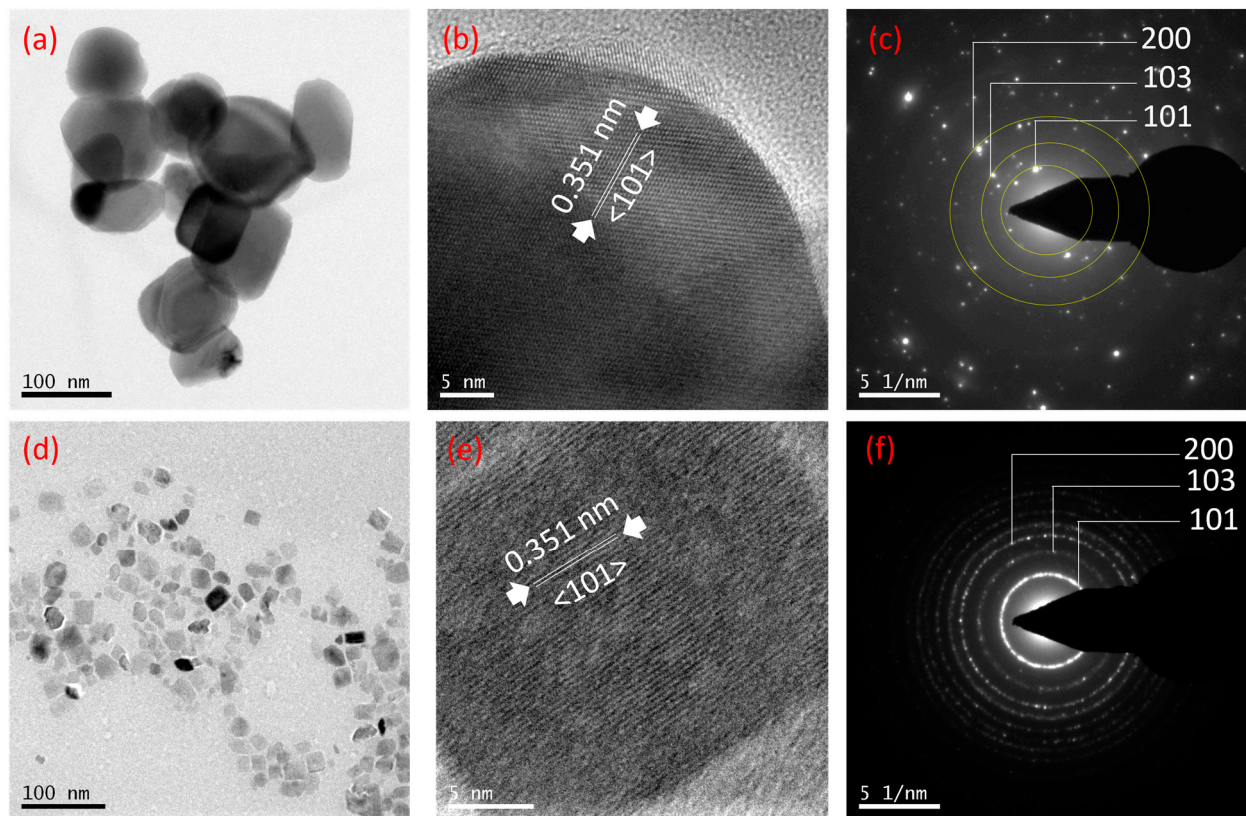
Figure 4. (**a**) TEM brightfield image, (**b**) corresponding HR-TEM image, and (**c**) SAED pattern of the commercial TiO_2 and (**d**) TEM bright-field image, (**e**) corresponding HR-TEM image, and (**f**) SAED pattern of the synthesized titania-synthesized TiO_2 samples.

The BET analysis was performed to determine the surface area of as-prepared NPs. A mesoporous type-IV isotherm with 71 m^2/g surface area was found for the synthesized material, whereas the commercial TiO_2 had a surface area of 32 m^2/g (Figure 5a). The higher surface area usually helps in enhancing the dye-loading behavior. Conversely, a large surface area can also increase the electron recombination process, negatively affecting the PV performance [52]. The pore size distribution, determined using the BJH method, is illustrated in the inset of Figure 5a. The commercial and synthesized TiO_2 samples show a distinct disparity in pore characteristics. The commercial TiO_2 exhibits a more defined distribution, ranging from 5 to 30 nm, with a peak at 20 nm, indicative of pore size

distortion. In contrast, the TNPs displays a broader range of pore sizes, spanning from 2 to 20 nm, with notable intensities within the 5–12 nm range, presenting a size distribution notably smaller than that of the commercial TiO_2. The observed variation in pore size is of substantial consequence, particularly in its influence on dye-loading and surface area distribution.
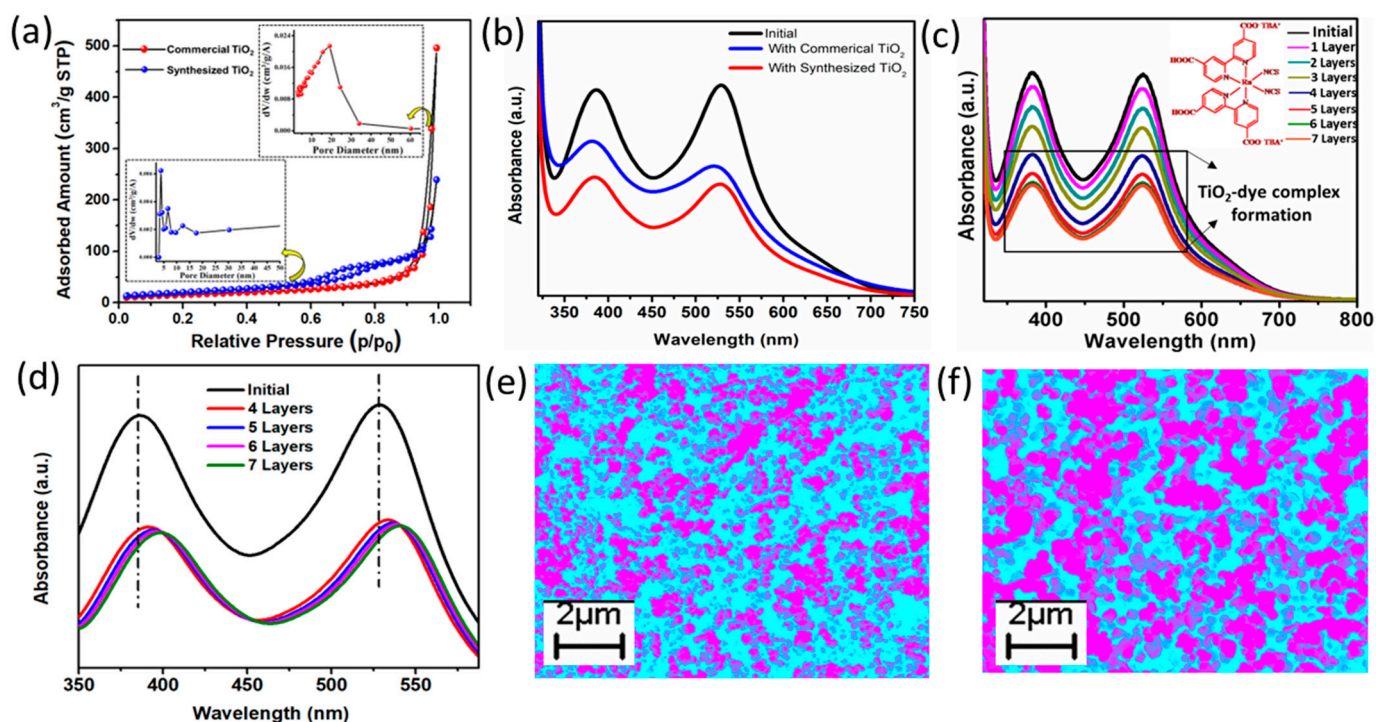
Figure 5. (**a**) The nitrogen absorption-desorption plot illustrates the synthesized TNP in comparison to commercial TiO_2 NPs, with the corresponding pore-size distribution plot shown in the inset, (**b**) UV-visible absorption spectroscopy plot displays N719 dye (inset: dye molecular structure) before and after dye-loaded with synthesized TNP, compared with commercial TiO_2 NPs, (**c**) UV-visible absorption spectroscopy plot demonstrates N719 dye loading during various layer-based TNP photoanodes. (**d**) A closer view of the UV-visible absorption spectroscopy plot reveals N719 dye loaded with more than 4 layers of the TNP photoanode, and (**e,f**) EDX dye loaded surface profiles of the 3 layers of TNP photoanodes are compared with commercial TiO_2 NPs. These images have been processed using MIPAR Image Analyzer software for enhanced color and contrast.

To understand more about the dye-loading behavior, the absorbance spectra were observed for both commercial and synthesized TiO_2 after dye-loading, as shown in Figure 5b. It indicates better dye-loading under reduced absorbance for the synthesized TNP, which was expected from the BET analysis. In Figure 5c, the investigation into the layer-dependent dye-loading performance of the TNP solar paint photoanode is presented through absorption spectroscopy. The dye-loading capacity exhibits an exponential relationship with the thickness of the TNP, represented by the number of layers. However, this relationship reaches a saturation level, and in our specific case, the saturation point is optimized after the deposition of 3 layers of TNP. This phenomenon is attributed to the slightly acidic nature of the dyes and TNP, fostering a robust formation of the Ti-dye complex [53].

Consequently, this interaction leads to dye agglomeration, as evidenced by a noticeable bathochromic shift in the original peak position of the dyes, as depicted in Figure 5d. Despite the favorable high dye-loading behavior, the observed bathochromic shift indirectly indicates Ti-dye complex formation. This aspect may not be conducive to enhancing the performance of DSSCs, particularly as it has the potential to diminish the fill factor and contribute to a decrease in short-circuit current. This is either due to non-uniform dye

absorption on the TiO$_2$ surface or randomly forming trapping or de-trapping states, thereby impacting the overall homogeneity of dye distribution.

A comparison was drawn between the dye-loading behavior of commercial TiO$_2$ and synthesized TNPs using the EDX mapping using the MIPAR image analyzer after 24 h of dye-loading for an approximately 4 μm-thick layer in each case. Figure 5d, for the commercial TiO$_2$ (Figure 5e), shows a relatively low dye-loading capacity compared to the TNP displayed in Figure 5f, where the more pink color represents more dye-loading. This behavior complements the expected trend from absorbance characteristics and surface area analysis.

The photographs depicted in Figure 6a,b illustrate the hydrothermally prepared sol before and after the hydrothermal treatment. Subsequently, the sol undergoes conversion into TNP solar paint, with Figure 6c presenting a visual representation of a single-layer brush-painted photoanode, dried at room temperature. A schematic is also given in Figure 6c to illustrate the electron transfer process in DSSC under illumination [54]. Upon exposure to light irradiation, dye molecules absorb photons with wavelengths corresponding to the energy differential between their highest occupied molecular orbital (HOMO) and lowest unoccupied molecular orbital (LUMO). This results in the elevation of electrons from the ground electronic state of the dye to the excited state (S*), constituting the photoexcitation of the dye. Subsequently, these photoexcited electrons are injected into the conduction band (CB) of the TNP. Upon injection into the CB of TNP, the electrons undergo diffusion through the semiconductor layer until they reach the transparent conducting layer on the FTO. At the anode, iodide ions (I$^-$) contribute electrons to oxidized dye species (S$^+$), thus regenerating the dye molecules. Simultaneously, the oxidized species of the electrolyte, triiodide (I$_3^-$), present in the iodide-triiodide (I$_2$/I$_3^-$) complex, is reduced to iodide at the cathode. This cyclic sequence of events ensures a continuous free electron flow through the external circuit, contingent upon incident light. Figure 6c illustrates the schematic representation of the various steps involved in a DSSC, elucidated through an energy level diagram. The alteration in electron concentration within the TNP induced by photo-initiated charge injection from the sensitized dye is the fundamental origin of photovoltage generation in a DSSC. The maximum open circuit voltage (V$_{OC}$) is dictated by the difference in electron energies between the redox level and the bottom of the conduction band of the electron conductor.
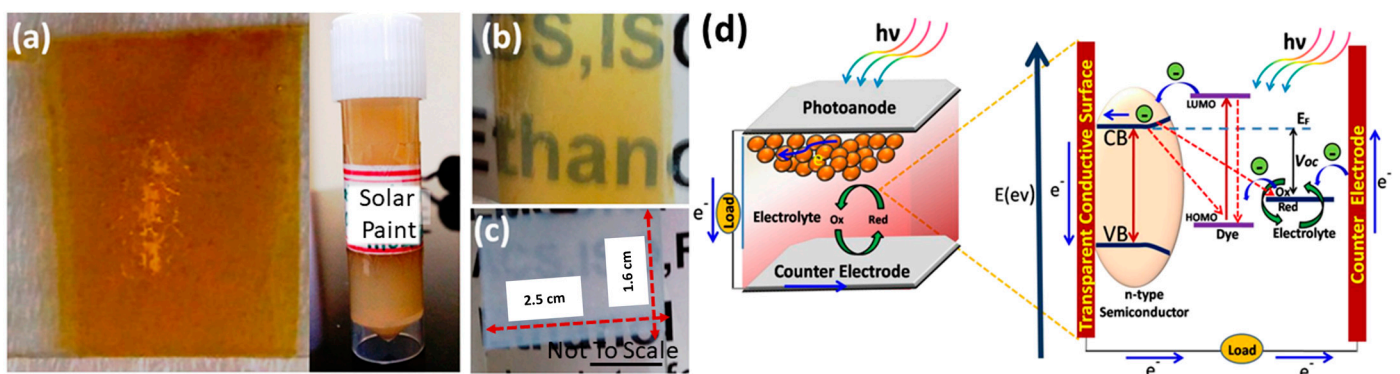
Figure 6. Hydrothermal sol of TNPs (**a**) before and (**b**) after hydrothermal treatment, respectively, (**c**) 1-step printed TNP solar paint, after room-temperature drying, and (**d**) schematic illustration of DSSC working principle.

However, the efficiency of DSSCs experiences a decline, primarily due to the following factors:

(a) Potential relaxation of electrons in the photoexcited dye to lower states of the chromophore or to its ground state.

(b) Slower reduction of I$_3^-$ at the counter electrode compared to its recombination with conduction band electrons of TNP.

(c) Accelerated recombination at the TNP/electrolyte interface relative to the diffusion of electrons through the TNP film, attributed to trapping states on the surface.

Given that the injection of electrons into the CB of TNP from the excited dye occurs rapidly within picoseconds, the efficiency of electron transport through the TNP film becomes pivotal in determining current collection efficiency.

Finally, the PV performances of the devices were examined, considering the effect of thickness from solar paint deposition for a 2.5×1.6 cm^2 active area. The devices were categorized into four sections depending on the number of TNP paint coatings, ranging from 1 to 4. The performances of the devices are shown in Figure 7a and Table 1, which indicate the best performance was the 3-layer coated DSSC (PCE of 6.02%), having a photoanode thickness of ~12 μm. On the other hand, one layer of TNP printing resulted in a PCE of 4.4%, along with a J_{SC} of 10.15 mA/cm^2, V_{OC} of 740 mV, and FF (fill factor) of 0.59. Similarly, two layers of photoanode printing resulted in a PCE of 5.22%, alongside a J_{SC} of 11.5 mA/cm^2, V_{OC} of 744 mV, and FF of 0.61. While testing the champion device with four printing layers, a current density of 11.6 mA/cm^2, open circuit voltage of 745 mV, FF of 62.5%, and PCE of 5.4% was observed. The devices' performance increased until the 3-layer coated DSSC, and then a decrease in performance was observed for the 4-layer device. This was expected as the higher thickness of the photoanode after a certain limit creates cracking, which influences the charge transport property by deteriorating the interfacial contact [55]. The performance was also compared with the commercially available high-temperature curing TiO$_2$ paste (12 μm-thick layer), and interestingly, the solar paint showed ~8% enhanced efficiency, which is remarkable for a larger device area. Further, electrochemical impedance spectroscopy (EIS) was carried out to realize the transport properties at different interfaces for the champion devices, having synthesized titania and commercial paste, as shown in Figure 7b. In the circuit diagram inset of Figure 7b, R_S represents the series resistances of FTO-glass and counter electrode at the high-frequency region. R_{ct-Pt} and Q_{ct-Pt} symbolize the resistance and double-layer capacitance of the Pt-FTO/electrolyte interface. $R_{ct-TiO_2/dye}$ and $Q_{ct-TNP/dye}$ signify the resistance and capacitance of the TNP-dye/electrolyte interface [56]. TThe EIS study observed that R_S for both commercial and lab-based TNP devices are almost similar, having a value of ~15 Ω. In contrast, R_{ct-Pt} for the tBA-based solar paint device was found to be ~46 Ω, which is nearly 12 Ω less than commercial TiO$_2$-based champion DSSC. Moreover, Figure 7b clearly depicts the $R_{ct-TiO_2/dye}$ value of the as-synthesized titania device as ~85 Ω, significantly higher than commercial titania-based DSSC. Usually, a DSSC device with a high V_{OC} value should have a higher charge transport resistance at the TNP /dye/electrolyte interface, which implies a reduced charge recombination rate [57]. Although the V_{OC} values are quite comparable for the commercial and synthesized TNP, the effect of reduced recombination is speculated to influence electron diffusion, which effectively enhances the current density of the solar paint-based DSSC. This explains the dominant performance of synthesized TNP due to the superior interface quality, which is a cumulative result of the structural property of the NPs, the standard of solar paint, and the screen-printing technique. Additionally, the reduced recombination phenomenon correlates with enhanced charge carrier diffusion. Expedited separation is feasible if electron diffusion across the photoanode thin film interface is efficient. Hence, a reduced micro-strain in the TNPs emerges as a vital parameter, suggesting that the synthesized TNPs demonstrate enhanced efficacy relative to conventional particles. Agglomeration typically results in mesoscale morphological structures, with the synthesized TNPs interconnected. Such connectivity amongst the NPs within a mesoscale entity is notably efficient.
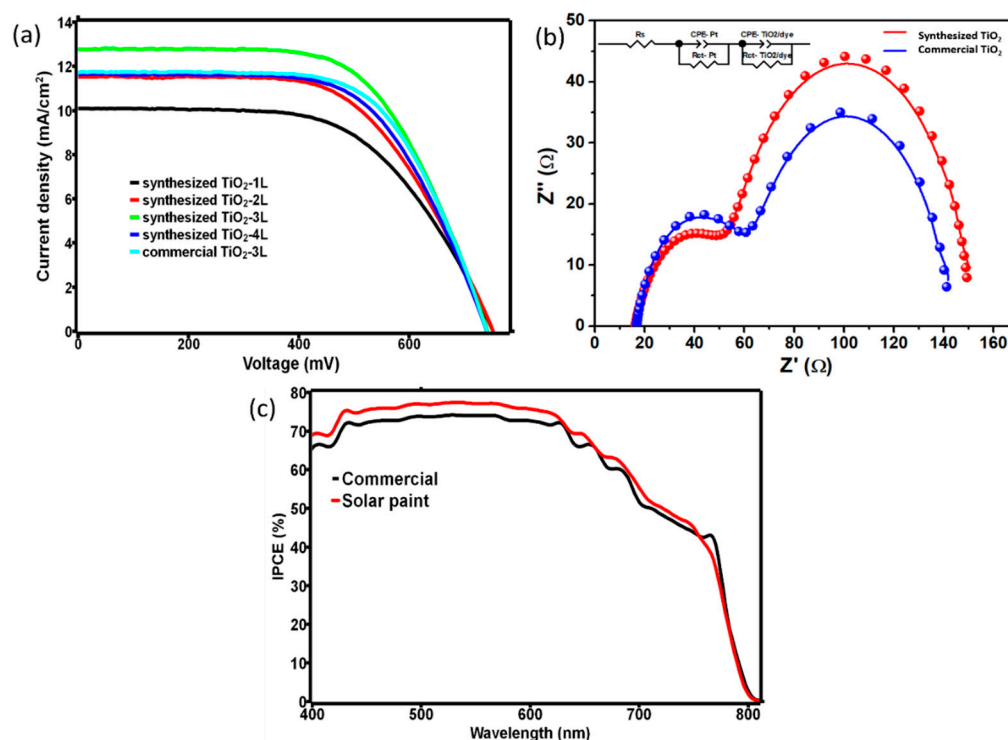
Figure 7. (a) Layer-dependent J-V curves of the champion devices of synthesized and commercial TNP, (**b**) comparative Nyquist plots with circuit diagram inset for the commercial and as-prepared TNP paste, and (**c**) IPCE plot of commercial and synthesized TNP-based champion DSSC compared with commercial TiO$_2$ paste.

Table 1. Comparative photovoltaic performance of champion devices fabricated by room-temperature solar paint and standard TiO$_2$ paste as photoanodes under 1 sun AM 1.5.

Photoanode	Current Density $\pm$ 0.5 (mA/cm^2)	V$_{OC}$ (mV)	FF	PCE (%) $\pm$ 0.2
RT-TNP Paste 1 L	10.15	740	0.59	4.4
RT-TNP Paste 2 L	11.5	744	0.61	5.22
RT-TNP Paste 3 L	12.75	749	0.63	6.02
RT-TNP Paste 4 L	11.6	745	0.625	5.4
High Temperature Curing TiO$_2$ paste	11.68	747	0.64	5.58

Figure 7c showcases the IPCE (EQE) spectra of the champion DSSCs based on the TNP solar paint and commercial TiO$_2$. The typical spectral response corresponding to the N719 dye, alongside the peak at around 530 nm, was observed for all DSSCs. However, the quantum efficiency maxima varied with the different types of photoanode systems. The DSSC with a 3-step brush painting using the TNP solar paint exhibited the highest maximum EQE (~79%), whereas the commercial titania-based DSSC displayed a slightly lower EQE of ~75%. The integrated J$_{SC}$ determined from the IPCE spectra closely matches the current-voltage measurement and follows the same trend as the maximum EQE. As IPCE is a cumulative result of light-harvesting, charge-injection, and charge-collection efficiencies, the impressive IPCE coverage for the anatase TiO$_2$ solar paint device in the ~400 to 650 nm range expresses significant superiority in interface quality and efficient charge carrier transport [58]. Finally, the stability of the DSSC devices was examined for 30 days at ambient conditions, and all the devices showed excellent retention of efficiency with only ~1% overall reduction. Stability majorly depends on the type of dye and electrolyte, which is the reason behind the similar trend. Overall, the performance amplification by

solar paint demonstrates a cheaper and easier alternative for the sustainable development of good-quality DSSC devices.]

4. Paste Commercialization Perspective

It is imperative to recognize that energy generation from renewable sources does not inherently ensure sustainability. Despite being derived from renewable sources, energy production still introduces emissions and challenges, notably using critical raw materials in associated technologies. Therefore, a comprehensive investigation into the key factors that jeopardize the sustainability of a particular technology is crucial for establishing renewable energy as genuinely sustainable. The most expensive constituents in DSSCs comprise the dye, TiO_2, and the glass/TCO substrate. In the case of the dye and TiO_2, the raw materials exhibit relatively low costs compared to the expenses incurred during the processing and synthesis phases. Ruthenium (Ru) constitutes only approximately 10% of the total dye cost. The remaining components of the dye molecule consist of inexpensive organics; however, the synthesis, ligand attachment, and subsequent purification processes contribute significantly to overall expenses. Plastic-based flexible DSSCs encounter challenges related to poor thermal stability, impeding the utilization of high-temperature sintering processes. This limitation hampers efforts to enhance inter-particle connections within the photoanode and promote adhesion between the photoanode and the plastic substrate. Consequently, the conversion efficiency of plastic-based flexible DSSCs lags behind that of rigid high-temperature DSSCs.

Scaling up the production of the dye from gram to kilogram volumes leads to a substantial reduction in price, diminishing from \$700/g to \$70/g. Similar cost reductions in processing are anticipated when production scales up to thousands of kilograms. While TiO_2 and raw Ti materials are abundant and economically viable, the hydrothermal synthesis of TiO_2 colloids is relatively costly. Hydrothermally prepared colloidal TiO_2 incurs a cost of approximately \$500/kg in ton quantities, representing a 30–50% increase over target production costs [59,60]. Alternative methods such as flame pyrolysis are more economical but sacrifice control over particle size and shape, resulting in generally lower efficiencies. The TCO-coated glass used in DSSCs is also a significant cost contributor. The glass per module area cost doubles for sandwich cells compared to monolithic modules. Anticipated economies of scale are expected to sufficiently lower the glass cost to acceptable levels when produced in high volumes. No technological breakthrough is deemed necessary in this regard. Furthermore, collaborations between glass companies and DSSC manufacturers can further reduce the cost of integrating TCO/glass into DSSC modules. Notably, no sustainable alternative to TiO_2 NPs has been proposed thus far due to their favorable characteristics, including a low recombination rate for hole–electron pairs, outstanding absorption properties, high chemical and thermal stability, corrosion resistance, non-toxicity, widespread availability, biocompatibility, and competitive cost. However, it is essential to acknowledge that certain properties of TiO_2 are not ideal, such as its 3.2 eV band gap in the anatase phase, leading to ultraviolet radiation absorption ($\lambda < 380$ nm), and the formation of highly reactive holes that can degrade specific device components. Despite these considerations, adopting alternative semiconducting oxides as photoanodes in DSSCs remains an area of active research. However, as far as we know, their performances have not surpassed those of TiO_2.

A primary focus of research involves the development of room-temperature curable TiO_2 electrodes in DSSCs, simply painted using a brush as a continuous film from a viscous paste. The preparation of TiO_2 paste involves using cheaper organic binders, which alter rheology for coating and introduce porosity in the thick film structure. This methodology presents significant advantages, reducing costs and enabling TiO_2 colloidal pastes to be the material of choice for roll-to-roll printing on flexible substrates. Moreover, these pastes exhibit efficiencies ~6% without sintering at high temperatures, offering versatility for application on polymer, glass, or metal foil substrates in DSSCs. Our developed TNP solar paint holds promising applications for large-scale roll-to-roll printing on flexible substrates,

significantly advancing in pursuing more commercially viable and scalable production. This is particularly advantageous for flexible DSSCs, which have demonstrated numerous benefits as solar devices. However, inherent limitations persist, especially in the case of plastic-based flexible DSSCs. In the broader context of DSSC research and development, specific directions are being pursued to impact module costs significantly. Exploration into dyes with higher extinction coefficients enhances efficiency and reduces costs by necessitating less dye and TiO$_2$ per module area. These research endeavors primarily influence the cost of supplied materials. Additionally, advancements in process integration and module design are anticipated to yield substantial benefits, further contributing to the overall improvement of DSSC technology.

Therefore, our TNP solar paint presents a feasible solution, as it eliminates the need for high-temperature sintering, mitigating a significant obstacle in the large-scale production of flexible solar devices. Moreover, the adaptability of our technology holds promise for improving the overall efficiency and cost-effectiveness of plastic-based flexible DSSCs. However, our preliminary findings indicate a promising trajectory towards the potential commercialization of TNP solar paint. Furthermore, it is imperative to conduct additional comprehensive studies and in-depth analyses to advance towards large-scale commercial application. These endeavors are essential for elucidating intricate nuances, refining existing parameters, and addressing potential challenges that may arise in the transition from preliminary feasibility to full-scale implementation. Pursuing a thorough understanding, informed by rigorous investigation and meticulous scrutiny, is paramount in substantiating the viability and robustness of the proposed commercialization strategy. Therefore, a strategic plan encompassing a series of meticulously designed studies and analyses must be systematically executed to fortify the foundation laid by our preliminary findings. This approach ensures a judicious progression towards realizing the envisioned commercial potential of the TNP solar paint. Besides, the statistical analysis of the dye-sensitized TNP solar paint is integral to comprehending and elucidating its performance characteristics. Employing a rigorous statistical approach allows for the extraction of meaningful insights and the establishment of robust correlations. Here, we present a statistical discussion focused on key parameters and their significance:

(i)   Particle Size Distribution:

Statistical analysis of the particle size distribution provides insights into the homogeneity of TiO$_2$ particles within the paste. Mean particle size, standard deviation, and skewness are essential parameters, offering a quantitative assessment of the paste's composition uniformity.

(ii)   Surface Area Analysis:

The specific surface area of TiO$_2$ particles is a critical factor influencing the paste's performance. Statistical measures such as mean surface area, variance, and confidence intervals contribute to a comprehensive understanding of the surface characteristics and, consequently, the paste's efficacy.

(iii)   Adhesion Strength:

Adhesion strength is a pivotal property determining the paste's suitability for applications. Employing statistical methods to assess adhesion, including mean adhesion strength and confidence intervals, allows for a reliable estimation of the paste's adherence to substrates.

(iv)   Electrochemical Performance:

Statistical analysis of electrochemical parameters, such as open-circuit voltage, short-circuit current, and fill factor, is imperative for evaluating the efficiency of the dye-sensitized TiO$_2$ paste. Regression analysis and hypothesis testing can be employed to identify significant factors influencing performance.

(v)   Optical Absorption Properties:

Statistical analysis of the optical absorption properties, including absorbance spectra and wavelength-dependent characteristics, provides valuable information regarding the paste's light-harvesting capabilities. Mean absorbance values and spectral trends are subject to rigorous statistical scrutiny.

(vi)   Durability and Stability:

Long-term performance and stability are crucial for practical applications. Statistical methods, such as survival analysis or accelerated testing, can be applied to assess the paste's durability under varying conditions, providing insights into its operational lifespan.

5. Conclusions

This study presents a comprehensive methodology for synthesizing a titania nanoparticle-based solar paint designed for facile curing at room temperature. Our approach focuses on the systematic sol-gel hydrothermal synthesis of ultrafine anatase TiO_2 NPs, subsequently utilized to formulate a solar paint amenable to processing at room temperature. We employed thorough microscopic and spectroscopic analyses to elucidate the structural attributes of the synthesized NPs. A critical assessment of dye-loading behavior, juxtaposed with commercial TiO_2, highlights the superior attributes of our synthesized material. We further underscore the efficacy of the screen-printing methodology for fabricating dye-sensitized solar cells (DSSCs) with a device area of 2.5 x 1.6 cm^2. Optimization studies reveal a photoanode thickness of 12 μm, resulting in a performance boost of approximately 36% relative to a 3 μm layer. A significant enhancement in PV performance is documented, with a remarkable efficiency of 6.02% for the solar paint. This improvement is primarily attributed to a pronounced reduction in the charge recombination process at the junction between the photoanode/dye and the electrolyte. This phenomenon is further elucidated through EIS and IPCE characterizations. The formulated solar paint has been advanced to manifest practical applicability in the facile fabrication of photoanodes at ambient temperatures. This innovative composition ensures superior surface uniformity devoid of organic binders. Notably, the formulation has been meticulously crafted to yield versatile porosity, thereby accommodating a spectrum of dye/electrolyte systems with efficacy.

Author Contributions: Conceptualization, A.R. and S.B.; Methodology, A.R., S.B. and T.S.; Validation, A.R. and S.B.; Formal analysis, A.R., S.B. and T.S.; Investigation, A.R., S.B. and T.S.; Data curation, A.R. and S.B.; Writing—original draft, A.R. and S.B.; Writing—review & editing, A.R., S.B. and T.S.; Visualization, A.R., S.B. and T.S. All authors have read and agreed to the published version of the manuscript.

Funding: This research received no external funding.

Institutional Review Board Statement: This study did not involve humans.

Informed Consent Statement: This study did not involve humans. Not applicable.

Data Availability Statement: The research data can be provided upon request to the corresponding author. The data are not publicly available due to Data are contained within the article.

Acknowledgments: AR would like to thank CSIR-CGCRI Kolkata for granting access to their material characterization facilities during his PhD studies. He also wishes to acknowledge the invaluable support he received from the Solar Energy Research Group at the University of Exeter, UK, for the photovoltaic characterizations conducted. For the purpose of open access, the author has applied a Creative Commons Attribution (CC BY) license to any Author Accepted Manuscript version arising.

Conflicts of Interest: The authors declare that they have no known competing financial interest or personal relationships that could have appeared to influence the work reported in this paper.

References

1. Chatterji, N.; Antony, A.; Nair, P.R. Temperature Coefficient of Silicon-Based Carrier Selective Solar Cells. *IEEE J. Photovolt.* **2019**, *9*, 583–590. [CrossRef]
2. Chander, S.; Purohit, A.; Sharma, A.; Arvind; Nehra, S.P.; Dhaka, M.S. A Study on Photovoltaic Parameters of Mono-Crystalline Silicon Solar Cell with Cell Temperature. *Energy Rep.* **2015**, *1*, 104–109. [CrossRef]
3. Lee, T.D.; Ebong, A.U. A Review of Thin Film Solar Cell Technologies and Challenges. *Renew. Sustain. Energy Rev.* **2017**, *70*, 1286–1297. [CrossRef]
4. Hermes, W.; Waldmann, D.; Agari, M.; Schierle-Arndt, K.; Erk, P. Emerging Thin-Film Photovoltaic Technologies. *Chem. Ing. Tech.* **2015**, *87*, 376–389. [CrossRef]
5. Bhandari, S.; Mallick, T.K.; Sundaram, S. Enlightening the Temperature Coefficient of Triple Mesoscopic $CH_3NH_3PbI_{3-x}Cl_x$/NiO and Double Mesoscopic $CsFAMAPbI_{3-x}Br_x$/CuSCN Carbon Perovskite Solar Cells. *J. Phys. Energy* **2023**, *5*, 25006. [CrossRef]
6. Mohammadian-Sarcheshmeh, H.; Arazi, R.; Mazloum-Ardakani, M. Application of Bifunctional Photoanode Materials in DSSCs: A Review. *Renew. Sustain. Energy Rev.* **2020**, *134*, 110249. [CrossRef]
7. Roy, A.; Ghosh, A.; Bhandari, S.; Selvaraj, P.; Sundaram, S.; Mallick, T.K. Color Comfort Evaluation of Dye-Sensitized Solar Cell (DSSC) Based Building-Integrated Photovoltaic (BIPV) Glazing after 2 Years of Ambient Exposure. *J. Phys. Chem. C* **2019**, *123*, 23834–23837. [CrossRef]
8. Tinker, L.; Jones-Albertus, R. Emerging PV Technologies: The Path to Market Competitiveness. In Proceedings of the 2016 IEEE 43rd Photovoltaic Specialists Conference (PVSC), Portland, OR, USA, 5–10 June 2016; pp. 3471–3474.
9. Zhang, W.; Ferguson, V.; Silva, S.R.P. Chapter 3—Nanocarbons for Emerging Photovoltaic Applications. In *Micro and Nano Technologies*; Ahmed, W., Booth, M., Nourafkan, E., Eds.; Elsevier: Amsterdam, The Netherlands, 2021; pp. 49–80, ISBN 978-0-12-821346-9.
10. Gong, J.; Sumathy, K.; Qiao, Q.; Zhou, Z. Review on Dye-Sensitized Solar Cells (DSSCs): Advanced Techniques and Research Trends. *Renew. Sustain. Energy Rev.* **2017**, *68*, 234–246. [CrossRef]
11. Roy, A.; Bhandari, S.; Sundaram, S.; Mallick, T.K. Intriguing CeO_2–TiO_2 Hybrid Nanostructured Photoanode Resulting up to 46% Efficiency Enhancement for Dye-Sensitized Solar Cells. *Mater. Chem. Phys.* **2021**, *272*, 125036. [CrossRef]
12. Mehmood, U.; Rahman, S.; Harrabi, K.; Hussein, I.A.; Reddy, B.V.S. Recent Advances in Dye Sensitized Solar Cells. *Adv. Mater. Sci. Eng.* **2014**, *2014*, 974782. [CrossRef]
13. Alizadeh, A.; Roudgar-Amoli, M.; Bonyad-Shekalgourabi, S.-M.; Shariatinia, Z.; Mahmoudi, M.; Saadat, F. Dye Sensitized Solar Cells Go beyond Using Perovskite and Spinel Inorganic Materials: A Review. *Renew. Sustain. Energy Rev.* **2022**, *157*, 112047. [CrossRef]
14. Barichello, J.; Mariani, P.; Matteocci, F.; Vesce, L.; Reale, A.; Di Carlo, A.; Lanza, M.; Di Marco, G.; Polizzi, S.; Calogero, G. The Golden Fig: A Plasmonic Effect Study of Organic-Based Solar Cells. *Nanomaterials* **2022**, *12*, 267. [CrossRef]
15. Mlinar, V. Engineered Nanomaterials for Solar Energy Conversion. *Nanotechnology* **2013**, *24*, 42001. [CrossRef]
16. Deshmukh, M.A.; Park, S.-J.; Hedau, B.S.; Ha, T.-J. Recent Progress in Solar Cells Based on Carbon Nanomaterials. *Sol. Energy* **2021**, *220*, 953–990. [CrossRef]
17. Das, P.P.; Roy, A.; Tathavadekar, M.; Devi, P.S. Photovoltaic and Photocatalytic Performance of Electrospun Zn_2SnO_4 Hollow Fibers. *Appl. Catal. B Environ.* **2017**, *203*, 692–703. [CrossRef]
18. Sugathan, V.; John, E.; Sudhakar, K. Recent Improvements in Dye Sensitized Solar Cells: A Review. *Renew. Sustain. Energy Rev.* **2015**, *52*, 54–64. [CrossRef]
19. Sharma, K.; Sharma, V.; Sharma, S.S. Dye-Sensitized Solar Cells: Fundamentals and Current Status. *Nanoscale Res. Lett.* **2018**, *13*, 381. [CrossRef] [PubMed]
20. Shin, S.S.; Suk, J.H.; Kang, B.J.; Yin, W.; Lee, S.J.; Noh, J.H.; Ahn, T.K.; Rotermund, F.; Cho, I.S.; Seok, S. Il Energy-Level Engineering of the Electron Transporting Layer for Improving Open-Circuit Voltage in Dye and Perovskite-Based Solar Cells. *Energy Environ. Sci.* **2019**, *12*, 958–964. [CrossRef]
21. Sheikh, M.S.; Roy, A.; Bhandari, S.; Mallick, T.K.; Sundaram, S.; Sinha, T.P. Highly Conductive Double Perovskite Oxides A_2LuTaO_6 (A = Ba, Sr, Ca) as Promising Photoanode Material for Dye Sensitized Solar Cells. *Mater. Lett.* **2020**, *276*, 128220. [CrossRef]
22. Meng, L.; Duwal, S.; Lane, J.M.D.; Ao, T.; Stoltzfus, B.; Knudson, M.; Park, C.; Chow, P.; Xiao, Y.; Fan, H.; et al. High Pressure Induced Atomic and Mesoscale Phase Behaviors of One-Dimensional TiO_2 Anatase Nanocrystals. *MRS Bull.* **2022**, *47*, 455–460. [CrossRef]
23. Cargnello, M.; Gordon, T.R.; Murray, C.B. Solution-Phase Synthesis of Titanium Dioxide Nanoparticles and Nanocrystals. *Chem. Rev.* **2014**, *114*, 9319–9345. [CrossRef] [PubMed]
24. Arunkumar, D.R.; Anjelin Ursula Portia, S.; Ramamoorthy, K. Design and Fabrication of Novel Tb Doped $BaTiO_3$ Thin Film with Superior Light-Harvesting Characteristics for Dye Sensitized Solar Cells. *Surf. Interfaces* **2021**, *22*, 100853. [CrossRef]
25. Lilge, T.S.; Ramires das Neves Stigger, A.; Fernandes, C.D.; Gularte, L.T.; Raubach, C.W.; da Silva Cava, S.; Gomes Jardim, P.L.; Giroldo Valerio, M.E.; Moreira, M.L. Increase of Voc Using Heterojunctions of $BaTiO_3$ without Sensitization. *Ceram. Int.* **2020**, *46*, 4907–4913. [CrossRef]
26. Yang, S.; Kou, H.; Wang, J.; Xue, H.; Han, H. Tunability of the Band Energetics of Nanostructured $SrTiO_3$ Electrodes for Dye-Sensitized Solar Cells. *J. Phys. Chem. C* **2010**, *114*, 4245–4249. [CrossRef]

27. Li, Y.; Zhang, H.; Guo, B.; Wei, M. Enhanced Efficiency Dye-Sensitized $SrSnO_3$ Solar Cells Prepared Using Chemical Bath Deposition. *Electrochim. Acta* **2012**, *70*, 313–317. [CrossRef]

28. Ebenezer Anitha, A.; Dotter, M. A Review on Liquid Electrolyte Stability Issues for Commercialization of Dye-Sensitized Solar Cells (DSSC). *Energies* **2023**, *16*, 5129. [CrossRef]

29. Singh, S.S.; Shougaijam, B. Recent Development and Future Prospects of Rigid and Flexible Dye-Sensitized Solar Cell: A Review. In *Contemporary Trends in Semiconductor Devices: Theory, Experiment and Applications*; Goswami, R., Saha, R., Eds.; Springer Nature: Singapore, 2022; pp. 85–109, ISBN 978-981-16-9124-9.

30. Yadav, S.C.; Sharma, A.; Devan, R.S.; Shirage, P.M. Role of Different Counter Electrodes on Performance of TiO_2 Based Dye-Sensitized Solar Cell (DSSC) Fabricated with Dye Extracted from Hibiscus Sabdariffa as Sensitizer. *Opt. Mater.* **2022**, *124*, 112066. [CrossRef]

31. Reale, A.; Cinà, L.; Malatesta, A.; De Marco, R.; Brown, T.M.; Di Carlo, A. Estimation of Energy Production of Dye-Sensitized Solar Cell Modules for Building-Integrated Photovoltaic Applications. *Energy Technol.* **2014**, *2*, 531–541. [CrossRef]

32. Mariani, P.; Vesce, L.; Di Carlo, A. The Role of Printing Techniques for Large-Area Dye Sensitized Solar Cells. *Semicond. Sci. Technol.* **2015**, *30*, 104003. [CrossRef]

33. Hussain, W.; Rashid, B.; Sridewi, N.; Ahmed, W.; Ahmad, M.S. Chapter 7—Development of Dye-Sensitized Solar Cell Module and Its Optimization. In *Dye-Sensitized Solar Cells*; Pandey, A.K., Shahabuddin, S., Ahmad, M.S., Eds.; Academic Press: Cambridge, MA, USA, 2022; pp. 137–157, ISBN 978-0-12-818206-2.

34. Arakawa, H.; Yamaguchi, T.; Takeuchi, A.; Agatsuma, S. Efficiency Improvement of Dye-Sensitized Solar Cell by Light Confined Effect. In Proceedings of the 2006 IEEE 4th World Conference on Photovoltaic Energy Conference, Waikoloa, HI, USA, 7–12 May 2006; Volume 1, pp. 36–39.

35. Dong, L.; Zheng, Z.; Wang, Y.; Li, X.; Hua, J.; Hu, A. Co-Sensitization of N719 with Polyphenylenes from the Bergman Cyclization of Maleimide-Based Enediynes for Dye-Sensitized Solar Cells. *J. Mater. Chem. A* **2015**, *3*, 11607–11614. [CrossRef]

36. Chatterjee, S.; Webre, W.A.; Patra, S.; Rout, B.; Glass, G.A.; D'Souza, F.; Chatterjee, S. Achievement of Superior Efficiency of TiO_2 Nanorod-Nanoparticle Composite Photoanode in Dye Sensitized Solar Cell. *J. Alloys Compd.* **2020**, *826*, 154188. [CrossRef]

37. Hashmi, S.G.; Özkan, M.; Halme, J.; Zakeeruddin, S.M.; Paltakari, J.; Grätzel, M.; Lund, P.D. Dye-Sensitized Solar Cells with Inkjet-Printed Dyes. *Energy Environ. Sci.* **2016**, *9*, 2453–2462. [CrossRef]

38. Hashmi, S.G.; Ozkan, M.; Halme, J.; Misic, K.D.; Zakeeruddin, S.M.; Paltakari, J.; Grätzel, M.; Lund, P.D. High Performance Dye-Sensitized Solar Cells with Inkjet Printed Ionic Liquid Electrolyte. *Nano Energy* **2015**, *17*, 206–215. [CrossRef]

39. Choudhury, M.S.H.; Ahmed Himu, S.E.; Khan, M.U.; Hasan, M.Z.; Alam, M.S.; Soga, T. Analysis of Charge Transport Resistance of ZnO-Based DSSCs Because of the Effect of Different Compression Temperatures. *AIP Adv.* **2023**, *13*, 95129. [CrossRef]

40. Cao, D.; Wang, A.; Yu, X.; Yin, H.; Zhang, J.; Mi, B.; Gao, Z. Room-Temperature Preparation of TiO_2/Graphene Composite Photoanodes for Efficient Dye-Sensitized Solar Cells. *J. Colloid Interface Sci.* **2021**, *586*, 326–334. [CrossRef] [PubMed]

41. Yamaguchi, T.; Tobe, N.; Matsumoto, D.; Nagai, T.; Arakawa, H. Highly Efficient Plastic-Substrate Dye-Sensitized Solar Cells with Validated Conversion Efficiency of 7.6%. *Sol. Energy Mater. Sol. Cells* **2010**, *94*, 812–816. [CrossRef]

42. Yin, X.; Xue, Z.; Wang, L.; Cheng, Y.; Liu, B. High-Performance Plastic Dye-Sensitized Solar Cells Based on Low-Cost Commercial P25 TiO_2 and Organic Dye. *ACS Appl. Mater. Interfaces* **2012**, *4*, 1709–1715. [CrossRef] [PubMed]

43. Agarkar, S.A.; Dhas, V.V.; Muduli, S.; Ogale, S.B. Dye Sensitized Solar Cell (DSSC) by a Novel Fully Room Temperature Process: A Solar Paint for Smart Windows and Flexible Substrates. *RSC Adv.* **2012**, *2*, 11645–11649. [CrossRef]

44. Maiti, D.; Saha, A.; Devi, P.S. Surface Modified Multifunctional $ZnFe_2O_4$ Nanoparticles for Hydrophobic and Hydrophilic Anti-Cancer Drug Molecule Loading. *Phys. Chem. Chem. Phys.* **2016**, *18*, 1439–1450. [CrossRef]

45. Mukhopadhyay, S.; Maiti, D.; Saha, A.; Devi, P.S. Shape Transition of TiO_2 Nanocube to Nanospindle Embedded on Reduced Graphene Oxide with Enhanced Photocatalytic Activity. *Cryst. Growth Des.* **2016**, *16*, 6922–6932. [CrossRef]

46. Zhao, Y.; Li, C.; Liu, X.; Gu, F.; Jiang, H.; Shao, W.; Zhang, L.; He, Y. Synthesis and Optical Properties of TiO_2 Nanoparticles. *Mater. Lett.* **2007**, *61*, 79–83. [CrossRef]

47. Rulison, A.J.; Miquel, P.F.; Katz, J.L. Titania and Silica Powders Produced in a Counterflow Diffusion Flame. *J. Mater. Res.* **1996**, *11*, 3083–3089. [CrossRef]

48. Song, Z.; Hrbek, J.; Osgood, R. Formation of TiO_2 Nanoparticles by Reactive-Layer-Assisted Deposition and Characterization by XPS and STM. *Nano Lett.* **2005**, *5*, 1327–1332. [CrossRef]

49. Li, J.-G.; Ikeda, M.; Ye, R.; Moriyoshi, Y.; Ishigaki, T. Control of Particle Size and Phase Formation of TiO_2 Nanoparticles Synthesized in RF Induction Plasma. *J. Phys. D Appl. Phys.* **2007**, *40*, 2348. [CrossRef]

50. Selvaraj, P.; Roy, A.; Ullah, H.; Sujatha Devi, P.; Tahir, A.A.; Mallick, T.K.; Sundaram, S. Soft-Template Synthesis of High Surface Area Mesoporous Titanium Dioxide for Dye-Sensitized Solar Cells. *Int. J. Energy Res.* **2019**, *43*, 523–534. [CrossRef]

51. Das, P.P.; Mukhopadhyay, S.; Agarkar, S.A.; Jana, A.; Devi, P.S. Photochemical Performance of ZnO Nanostructures in Dye Sensitized Solar Cells. *Solid. State Sci.* **2015**, *48*, 237–243. [CrossRef]

52. Zhu, K.; Kopidakis, N.; Neale, N.R.; van de Lagemaat, J.; Frank, A.J. Influence of Surface Area on Charge Transport and Recombination in Dye-Sensitized TiO_2 Solar Cells. *J. Phys. Chem. B* **2006**, *110*, 25174–25180. [CrossRef] [PubMed]

53. Lee, K.E.; Gomez, M.A.; Elouatik, S.; Demopoulos, G.P. Further Understanding of the Adsorption Mechanism of N719 Sensitizer on Anatase TiO_2 Films for DSSC Applications Using Vibrational Spectroscopy and Confocal Raman Imaging. *Langmuir* **2010**, *26*, 9575–9583. [CrossRef]

54. Lamberti, A.; Sacco, A.; Bianco, S.; Manfredi, D.; Cappelluti, F.; Hernandez, S.; Quaglio, M.; Pirri, C.F. Charge Transport Improvement Employing TiO$_2$ Nanotube Arrays as Front-Side Illuminated Dye-Sensitized Solar Cell Photoanodes. *Phys. Chem. Chem. Phys.* **2013**, *15*, 2596–2602. [CrossRef]

55. Taleb, A.; Mesguish, F.; Yanpeng, X. Effect of Cracking and Aggregation on the Efficiency of DSSC. In Proceedings of the 2014 International Renewable and Sustainable Energy Conference (IRSEC), Ouarzazate, Morocco, 17–19 October 2014; pp. 46–51.

56. Omar, A.; Ali, M.S.; Abd Rahim, N. Electron Transport Properties Analysis of Titanium Dioxide Dye-Sensitized Solar Cells (TiO$_2$-DSSCs) Based Natural Dyes Using Electrochemical Impedance Spectroscopy Concept: A Review. *Sol. Energy* **2020**, *207*, 1088–1121. [CrossRef]

57. He, J.; Guo, F.; Li, X.; Wu, W.; Yang, J.; Hua, J. New Bithiazole-Based Sensitizers for Efficient and Stable Dye-Sensitized Solar Cells. *Chem.—A Eur. J.* **2012**, *18*, 7903–7915. [CrossRef] [PubMed]

58. Shin, S.S.; Kim, J.S.; Suk, J.H.; Lee, K.D.; Kim, D.W.; Park, J.H.; Cho, I.S.; Hong, K.S.; Kim, J.Y. Improved Quantum Efficiency of Highly Efficient Perovskite BaSnO$_3$-Based Dye-Sensitized Solar Cells. *ACS Nano* **2013**, *7*, 1027–1035. [CrossRef] [PubMed]

59. Rahman, S.; Haleem, A.; Siddiq, M.; Hussain, M.K.; Qamar, S.; Hameed, S.; Waris, M. Research on Dye Sensitized Solar Cells: Recent Advancement toward the Various Constituents of Dye Sensitized Solar Cells for Efficiency Enhancement and Future Prospects. *RSC Adv.* **2023**, *13*, 19508–19529. [CrossRef] [PubMed]

60. Kokkonen, M.; Talebi, P.; Zhou, J.; Asgari, S.; Soomro, S.A.; Elsehrawy, F.; Halme, J.; Ahmad, S.; Hagfeldt, A.; Hashmi, S.G. Advanced Research Trends in Dye-Sensitized Solar Cells. *J. Mater. Chem. A* **2021**, *9*, 10527–10545. [CrossRef]